https://doi.org/10.1590/jatm.v18.1435 ORIGINAL PAPER

Hydrodynamic Analysis of Amphibious Aircraft Stability during Water Taxiing

Li Zhandong[1,*], Zhang Feifan[1], Kong Fanwei[2], Qu Ligang[1], Zhao Jinfang[1]

1.Shenyang Aerospace University – Civil Aviation School – Shenyan – China.
2.School of Aeronautics and Astronautics – Shenyang Aerospace University – Shenyang – China.

*Corresponding author: lizhandong365@163.com

ABSTRACT

Waves can impair the gliding stability of amphibious aircraft on the water. This study employed numerical modeling to investigate the hydrodynamics of aircraft floats. Hydrodynamic forces were evaluated for different float cross-sections using the volume of fluid (VOF) method. The influence of wave properties on gliding stability was also investigated, along with forces during accelerated taxiing and the role of the acceleration coefficient. By comparing pressure and vortex patterns, the effect mechanism of wave height and wavelength on the stability was clarified. The findings indicate that the stability is highly sensitive to the position of the wave crest impact relative to the center of gravity. An impact near the center of gravity can cause instability with a wave height of 0.5 m and a wavelength of 5 m. Moreover, the accelerated taxiing exerts the most substantial influence on aircraft stability, potentially triggering roll and pitch motions. These findings offer key theoretical support for the design and optimization of amphibious aircraft floats.

Keywords: Amphibious aircraft float; Numerical simulation; Waves; Motion stability.

INTRODUCTION

Light amphibious aircraft (Che, 2022) represent a specialized category of aviation platforms capable of operating from both terrestrial runways and water surfaces. Their defining characteristic is the ability to perform amphibious take-offs, landings, and taxiing without restriction. These aircraft are further distinguished by low noise emissions, excellent low-altitude flight performance, and high energy efficiency. Such capabilities make them well-suited for a variety of applications (Huang 2018; Lin 2010), including recreational water excursions, waterway transportation, and emergency rescue operations. Most light amphibious aircraft employ a twin-float configuration, which is critical to their marine operation. During water taxiing, these floats interact directly with wave conditions, significantly influencing the aircraft's hydrodynamic stability.

With advances in computational methods, numerical simulation has become an essential tool for analyzing amphibious aircraft stability during taxiing. Duan (2019) investigated unsteady hydrodynamics during take-off, demonstrating that pitch and yaw motions are predominantly governed by hydrodynamic forces, with aerodynamics playing a secondary role. Huang (2015; 2016; 2018) conducted experimental studies on amphibious aircraft hydrodynamics, leading to design improvements. Li (2019; 2020a; b) examined challenges in high-speed gliding, including pronounced motion responses and strong flow field nonlinearities. Zeng *et al.* (2015) numerically simulated landings on regular waves, quantifying the influence of wavelength and height, while Hu *et al.* (2020) concluded that waves significantly affect longitudinal motion responses. Zhang *et al.* (2018) simulated take-off taxiing at fixed attitudes using ANSYS, and Ju *et al.* (2020) employed the finite volume method to study impact and gliding on wavy surfaces.

Received: Jul. 7, 2025 | **Accepted:** Mar. 13, 2026
Peer Review History: Single Blind Peer Review.
Section editor: Paulo Greco

Ma *et al.* (2018) developed a dynamic regular wave model using a moving boundary method and simulated landings with variable descent speeds and wave positions. Shi (2024) analyzed motion responses under various wave conditions, accelerations, and initial landing speeds. Li *et al.* (2023) performed a detailed hydrodynamic analysis using the Navier-Stokes equations, resolving non-uniform flow fields. Lv *et al.* (2023) studied the effects of wave conditions and landing methods on structural loads. Sun *et al.* (2024) identified that wave-induced drag correlates with wave height, wavelength, taxiing speed, and center of gravity position – a finding corroborated by Zhou *et al.* (2023), who further analyzed the influence of different wave components on stability. Chen *et al.* (2022) compared wave landing performance with hydrostatic conditions, noting increased impact loads and reduced safety with greater wave heights.

Current research on amphibious aircraft hydrodynamics predominantly focuses on hull-type configurations, whose hydrodynamic mechanisms fundamentally differ from twin-float designs, limiting the applicability of existing findings. Particularly for light twin-float amphibious aircraft, the stability mechanisms under coupled wave and accelerated taxiing conditions remain poorly understood, while existing numerical methods exhibit limitations in wave simulation and motion control. To address these gaps, this study developed a numerical simulation approach incorporating a user-defined function (UDF)-controlled acceleration, enabling precise modeling of float dynamics during variable-speed taxiing in wave environments. This method overcomes the constraints of traditional wave-generation techniques by integrating open-channel wave generation, allowing systematic analysis of the effects of wave height, wavelength, and acceleration coefficients on float hydrodynamic performance and stability. Through comparative analysis of resistance, lift, and vortex structures, key conditions leading to float instability in waves were identified. The findings provide theoretical support for the design and operation of twin-float amphibious aircraft.

This paper quantifies and analyzes the effects of wave parameters on hydrodynamic forces and stability. The work is structured as follows: first, the structural parameters of the amphibious aircraft are outlined. Subsequently, the numerical methodology employed to simulate the hydrodynamics of the floats is described. Finally, the results under various wave conditions and acceleration profiles are presented, elucidating the underlying mechanisms governing the hydrodynamic response. Finally, the key conclusions are summarized.

Amphibious aircraft

The evolution of amphibious aircraft has progressed through several distinct phases. In the early 20th century, models such as the Curtiss model and the Dornier Wal demonstrated the initial realization of amphibious functionality, marking the transition from conceptual design to practical operation. These early designs incorporated floats and metal structures to enhance airworthiness and durability.

During the 1930s and 1940s, amphibious aircraft entered a period of rapid development, particularly in military applications. Aircraft such as the PBY Catalina and the Short Sunderland featured extended range, increased payload capacity, and enhanced defensive capabilities, enabling operation in complex combat environments.

In the post-World War II era, the role of amphibious aircraft expanded into civilian sectors, with designs such as the Grumman HU-16 Albatross and ShinMaywa US-1 offering improved seaworthiness and mission versatility. In the modern era, emphasis has shifted toward multifunctional mission capability. Models such as the Beriev Be-200 and AVIC AG600 incorporate jet propulsion and advanced materials, with the latter representing a significant milestone in terms of scale and performance. Future developments are expected to focus on energy efficiency, reduced environmental impact, and integration of artificial intelligence to meet increasingly diverse operational requirements.

A lightweight electric two-seat amphibious aircraft has recently been developed at Shenyang Aerospace University (Fig. 1). Its design prioritizes weight reduction and extended flight range, with key structural and performance parameters provided in Table 1.

The float is a critical component of an amphibious aircraft, playing a significant role in both its hydrodynamic and aerodynamic performance. Its hull design directly influences seakeeping behavior and glide performance. In this study, the float model validated by Zhao *et al.* (2021) and illustrated in Fig. 2 is adopted. Key hull parameters are summarized in Table 2.

Source: Elaborated by the authors.

Figure 1. A lightweight electric two-seater amphibious aircraft.

Table 1. Specific parameters of the amphibious aircraft model.

Parameter	Value	Parameter	Value
Wing span (m)	14.50	Height (m)	3
Leight (m)	6.81	Maximum take-off weight (kg)	650
Payload (kg)	160	Maximum endurance (h)	1
Maximum flight range (km)	120	Maximum level flight speed (km·h)	165
Stall speed (km·h)	≤ 90	Cruising speed (km·h)	100
Flight duration (min)	≥ 75	Cruising altitude (m)	1000
Range (km)	≥125	G-loads (g)	+3.33, -1.66
CG (m)	(2.20, 0, 0)	Volume (m^3)	4.96

Source: Elaborated by the authors.

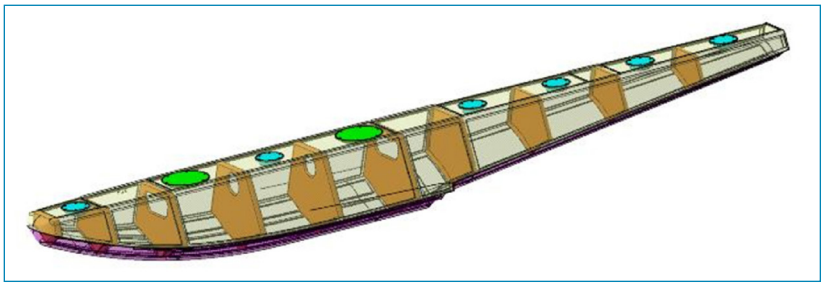

Source: Elaborated by the authors.

Figure 2. A float model of an amphibious aircraft.

Table 2. The hull parameters of the float.

Parameters	Value	Parameters	Value
Maximum width (m)	0.54	Front body length (m)	2.30
Rear body length (m)	2.10	Total length (m)	4.40
Step height (mm)	30	Volume (m^3)	0.54

Source: Elaborated by the authors.

Computational fluid dynamics (CFD) simulation

Numerical method

The hydrodynamic forces acting on the amphibious aircraft float are predicted by solving the unsteady, three-dimensional Navier-Stokes equations using CFD.

As illustrated in Fig. 3, the computations are performed within a rectangular domain measuring 4.5 L × 2.4 L × 3.5 L (length × width × height), where L represents the float length. The float is positioned 1.2 L from the inlet (left boundary) and 2.3 L from the outlet (right boundary). The distances to the other boundaries are set to 1.14 L.

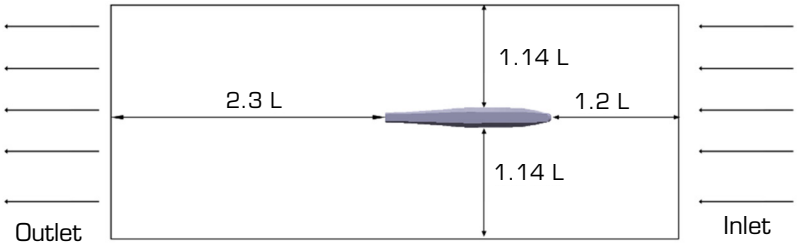

Source: Elaborated by the authors.

Figure 3. The computational domain containing floats.

The computational domain was discretized using an unstructured grid, as shown in Fig. 4. The mesh was refined around the float, and prismatic boundary layer grids were generated to resolve the near-wall flow structures, thereby ensuring accurate capture of the key flow field characteristics.

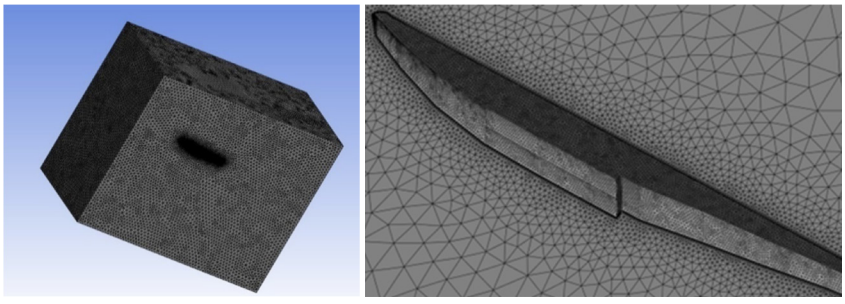

Source: Elaborated by the authors.

Figure 4. Integral mesh and encrypted mesh of the float.

The boundary conditions for the three-dimensional computational domain are defined as follows: the left face is set as a velocity inlet, the top and right faces as pressure outlets, and the cross-sectional face is assigned as a symmetry plane (Fig. 5). The remaining surfaces are defined as walls. To model the hydrodynamics of the float, a multiphase flow approach is employed, initializing the region above the float with air and the remainder with water.

The turbulence in the numerical simulation is modeled using the κ-epsilon model with standard wall functions. A multiphase flow is defined by partitioning the domain into air and water phases. The reference air pressure is set to standard atmospheric pressure, and gravitational acceleration is specified as 9.81 $m \cdot s^{-2}$. The volume of fluid (VOF) method is employed to track the air-water interface, with a surface tension coefficient of 0.072 $N \cdot m^{-1}$ applied to capture the free surface dynamics. Waves are generated using the VOF open-channel wave model and dissipated numerically using a damping zone to minimize reflection. Pressure-velocity coupling is handled via the coupled algorithm. Spatial discretization uses a first-order upwind scheme for pressure and a second-order upwind scheme for momentum.

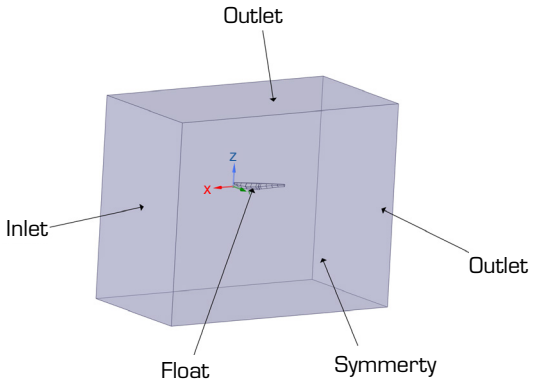

Source: Elaborated by the authors.

Figure 5. The boundary conditions of a computational domain.

Independence of grid and time-step

The computational domain is discretized using the finite volume method, the established approach for CFD applications. Solution accuracy is strongly influenced by mesh resolution. While a coarse mesh may yield imprecise results, an excessively refined mesh captures flow details at the cost of prohibitive computational expense. Therefore, selecting a mesh of appropriate density is essential.

A grid independence study was conducted using three systematically refined grids (coarse, medium, and fine), with key parameters summarized in Table 3. This analysis ensures that the chosen mesh achieves an optimal balance between numerical accuracy and computational efficiency.

Table 3. Specific parameters of three types of grid.

Grid	Number of grids	Additional layer grid size (m)	Flow field size (m)
Coarse grid	1.07×10^6	0.05	0.30
Medium grid	1.55×10^6	0.02	0.28
Fine grid	2.05×10^6	0.02	0.25

Source: Elaborated by the authors.

The hydrodynamic drag on the float at $v = 8$ m·s^{-1} was computed using three mesh densities. The transient drag history is presented in Fig. 6, while Table 4 summarizes the mean drag values and the relative errors of the coarse and fine mesh solutions with respect to the medium mesh baseline.

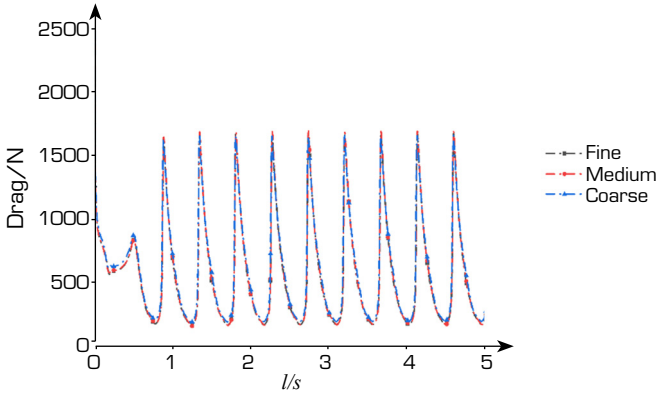

Source: Elaborated by the authors.

Figure 6. The transient drag of three types of grid density.

Table 4. Comparison of average drag and error for different grids.

Kinds of mesh	Grid number (W)	Drag (n) (N·m^{-1})	Error (%)
Coarse grid	100	595.38	4.89
Medium grid	150	567.57	Base data
Fine mesh	200	562.17	0.95

Source: Elaborated by the authors.

The grid independence study confirms that the variation in resistance across mesh densities remains below 5%. The close agreement between the medium and fine mesh solutions, particularly in mean drag, verifies that the results are independent of further grid refinement. Consequently, the medium mesh was selected for all subsequent simulations.

The choice of time-step is critical to both the stability and efficiency of the transient simulation. An overly large time step may induce numerical instability, while an excessively small one unnecessarily increases computational cost. To determine an appropriate value, the average drag on the float at 10 m·s^{-1}was computed using time-steps of $\Delta t = 0.05\ T$, $0.005\ T$, and $0.0025\ T$. The resulting drag values and their relative errors are summarized in Table 5, demonstrating the influence of temporal discretization.

The sensitivity of solution accuracy to time-step size is demonstrated in Table 5. As the time step decreases, the numerical error diminishes accordingly. Based on a balance between computational cost and result precision, a time-step of $t = 0.005\ T$ was selected for all subsequent simulations.

Table 5. Comparison of average drag and error for different time steps.

Step-time (T)	Drag (n)	Error (%)
0.05	858.3	7.68
0.005	797.03	Base data
0.0025	788.29	1.09

Source: Elaborated by the authors.

Method verification

To validate the present numerical approach, simulations were performed using the Wigley hull, a standard mathematical form with a slender geometry analogous to the float studied here. Experimental data from reference (Kajitani *et al.* 1983) were used for comparison. The principal parameters of the monohull Wigley model are listed in Table 6.

Table 6. Parameters of the monohull Wigley vessel type.

Length *L* (m)	Breadth *B* (m)	Draft *D* (m)	Volume *V* (m^3)
2.50	0.25	0.16	0.08

Source: Elaborated by the authors.

To further validate the feasibility of the proposed method, this study compares its results with those from a 1:3 scaled integrated model test conducted by the Liaoning General Aviation Research Institute at Shenyang Aerospace University (the physical model used in the test is consistent with the simulation model). The configuration of the static water towing test setup is shown in Figs. 7 and 8. A comparison of the relevant experimental parameters and an analysis of the data errors under the operating condition of a towing speed $v = 6$ m·s^{-1} and an attitude angle of 1.6° are presented in Table 7.

As shown in Table 7, under the same model scale and operating conditions, all computed parameters from the hydroplaning simulation exhibit errors within 10%. These results validate the effectiveness of the numerical method established in the Numerical method Section.

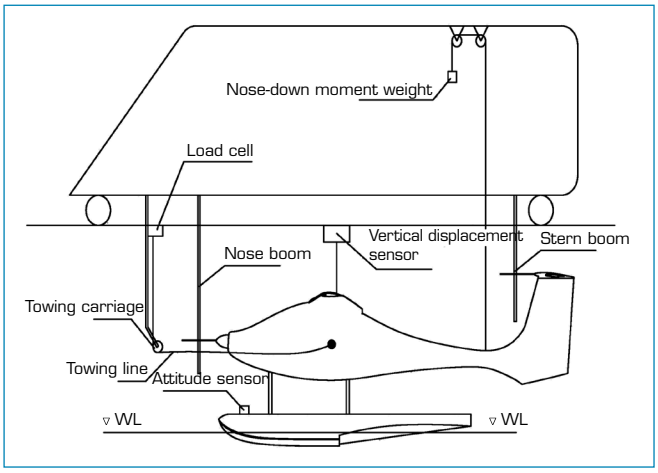

Source: Elaborated by the authors.

Figure 7. Schematic of the towing tank facility and measurement system.

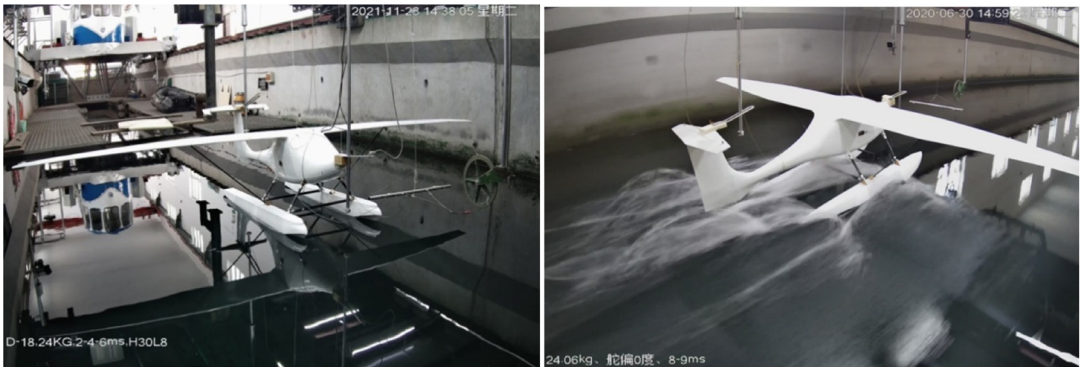

Source: Elaborated by the authors.

Figure 8. Field documentation of the hydrodynamic test procedure.

Table 7. Comparison of experimental and simulation results at a towing speed of 6 m·s^{-1} and an attitude angle of 1.6°.

Parameter	Drag (n)	Heave (mm)	Trim angle (°)
Experimental value	51.85	64.70	9.23
Calculated value	53.05	59.79	9.71
Error (%)	2.30	-7.58	5.23

Source: Elaborated by the authors.

RESULTS

When an amphibious aircraft glides on the water surface, the wave acts on the float, and is mathematically modeled by the shallow/intermediate waves. According to Airy wave theory, i.e., a linear Airy wave theory model, the equation for the wavefront is represented by:

$$\eta(x,t) = \alpha \cos(\kappa x - \omega t) \tag{1}$$

Where α, κ, x, t, and ω denote the wave amplitude, wave number, spatial coordinate in the x-direction, time, and angular frequency, respectively.

As expressed in Eq. 1, the wave profile follows a cosine function periodic in the x-direction. First-order Airy wave theory, which satisfies the linear wave assumptions of small amplitude, is well-suited for preliminary analysis of small-amplitude wave conditions.

Influence of wave height on the stability

The glide stability of floats in wave conditions represents a critical research focus for light electric amphibious aircraft operations. Wave height significantly influences float stability, and numerical simulations were conducted to systematically evaluate its effect on hydrodynamic performance.

The simulation setup maintained the following conditions: a gliding speed of 10 m·s^{-1}, wavelength of 5 m, fixed attitude angle of 6°, submersion depth of 0.75 h (where h is the float height), and wave propagation normal to the computational domain inlet. Hydrodynamic forces were computed across wave heights ranging from 0.1 m to 1.8 m, with the results presented in Figs. 9 and 10.

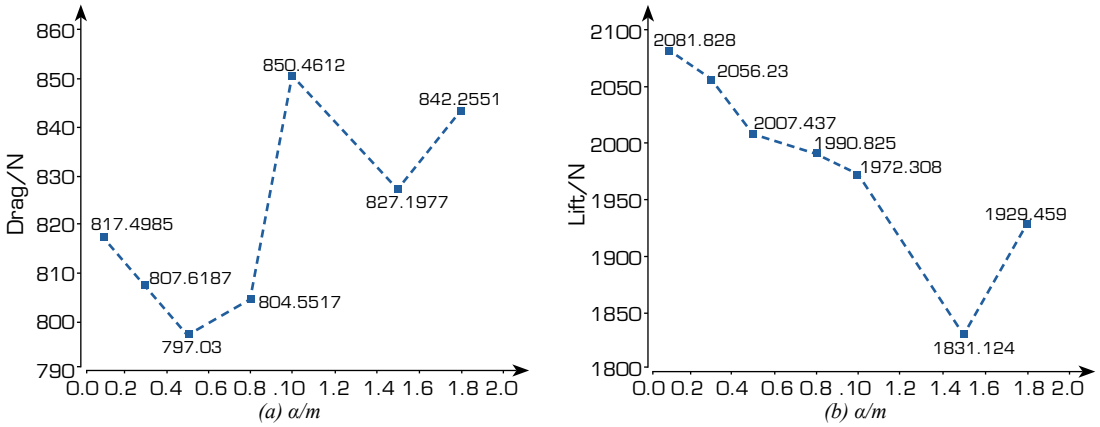

Source: Elaborated by the authors.

Figure 9. Comparison of mean hydrodynamic forces under different wave heights (l = 5 m, velocity = 10 m·s^{-1}). (a) Drag; (b) Lift.

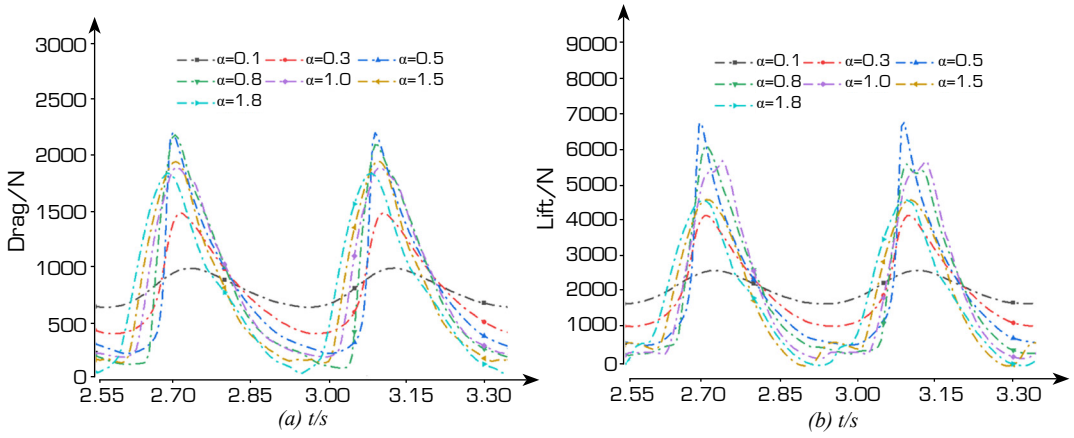

Source: Elaborated by the authors.

Figure 10. Evolution of transient forces under varying wave conditions (l = 5 m, v = 10 m·s^{-1}). (a) Drag; (b) Lift.

Figure 9 shows that the average drag first decreases at wave heights below 0.5 m, increases steadily between 0.5 m and 1 m, and declines again from 1 m to 1.5 m. The lift decreases up to 1.5 m, beyond which it rises. As shown in Fig. 10, both the drag and lift exhibit periodic variations. When waves strike the float – especially at the wave crest – both forces increase sharply, with the lift increasing more significantly than the drag. This indicates that wave effects on lift are more pronounced than those on drag during gliding. The maximum values of both drag and lift occur at a wave height α of 0.5 m.

Figure 11 compares the two-phase flow contours at α = 0.5 m and 0.8 m at t = 2.7 s. At α = 0.5 m, the wave crest acts directly near the float's center of gravity, causing a sharp rise in both drag and lift. The pressure distribution on the float bottom at α = 0.5 m (Fig. 12)

is more concentrated near the center of gravity compared to α = 0.8 m. At this wave height, the contact area between the trough and the float is minimal, resulting in the lowest overall drag. As the wave height increases from 0.5 m to 1 m, the wave remains lower than the float's vertical height, leading to increased drag. Beyond 1 m, the wave exceeds the float height, reducing the contact area between the crest and trough, and thus the drag decreases. Additionally, the trough position influences buoyancy, contributing to drag variations. These results demonstrate that wave geometry relative to the float's center of gravity strongly affects hydrodynamic response. To maintain glide stability, wave heights should be controlled to avoid strong wave action near the center of gravity, which can induce large drag fluctuations.

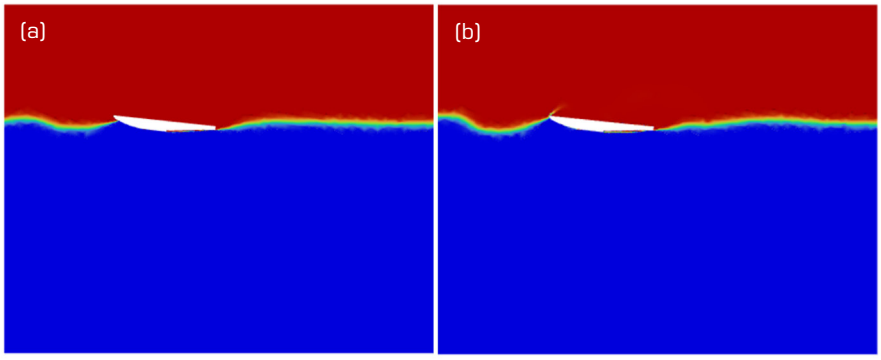

Source: Elaborated by the authors.

Figure 11. Comparison of air-water interfaces during crest passage under different wave heights: (a) α = 0.5 m; (b) α = 0.8 m.

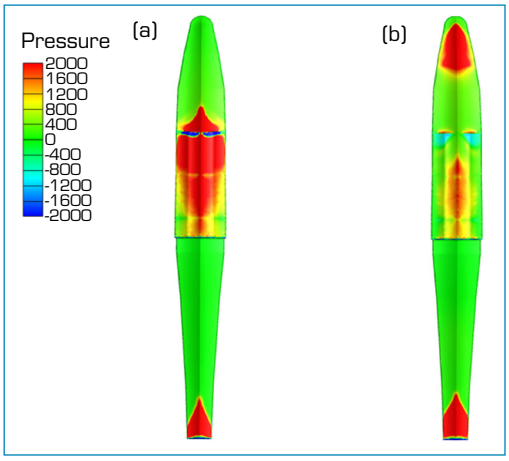

Source: Elaborated by the authors.

Figure 12. Comparative analysis of bottom pressure contours under varying wave heights. (a) α = 0.5 m; (b) α = 0.8 m.

Furthermore, Fig.13 shows that the clockwise vortex at the float's head is more pronounced at α = 0.5 m than at α = 0.8 m. This stronger vortex induces an intensified upward-surge flow, which contributes to the increases in drag and lift. In contrast, the counterclockwise vortex at the tail is more dominant at α = 0.8 m. This vortex structure disturbs the surrounding flow, altering its velocity and direction, thereby adversely affecting aircraft stability and handling.

The two-phase flow and vorticity fields at α = 1.5 m are shown in Figs. 14 and 15. At this wave height, which exceeds the float's own height, clockwise vortex structures form at its stern. The associated pressure alteration at the tail induces a submerged tendency, causing the float to adopt a longitudinal trim. This posture, in turn, promotes the generation of negative lift.

In summary, the wave height should not exceed the float height during gliding operations. Variations in wave height across different phases significantly influence glide stability. Effective wave management is essential to prevent excitation of the center of gravity, which would otherwise induce longitudinal instability.

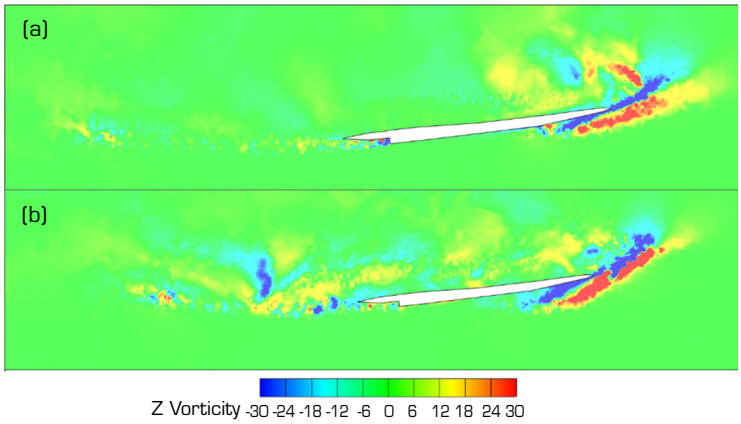

Source: Elaborated by the authors.

Figure 13. Evolution of vorticity contours at t = 5 s under different wave conditions. α = 0.5 m; (b) α = 0.8 m.

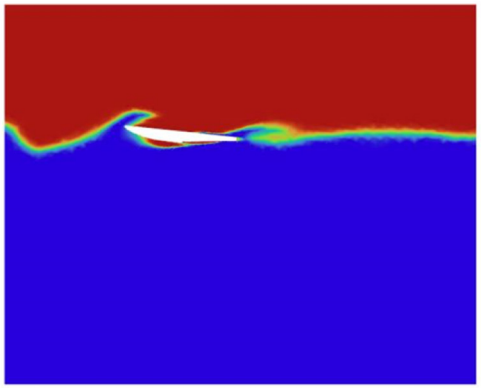

Source: Elaborated by the authors.

Figure 14. Instantaneous air-water interface during wave gliding (t = 5 s, α = 1.5 m).

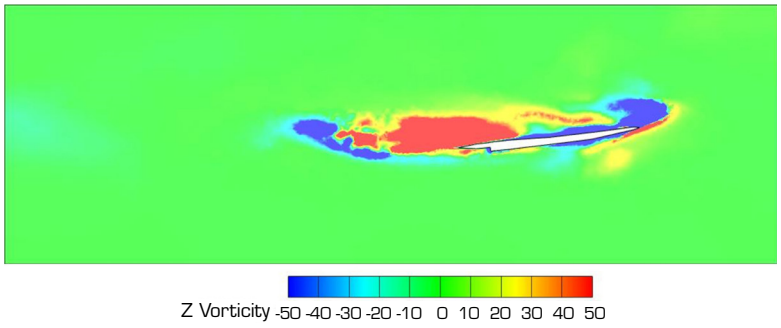

Source: Elaborated by the authors.

Figure 15. Development of vortex structures at t = 5 s under α = 1.5 m wave height.

Influence of wavelength on the stabilities

Wavelength serves as a fundamental parameter in the wave function and is directly related to wave propagation velocity. Moreover, waves with longer wavelengths exhibit greater resistance to local disturbances and maintain more stable propagation characteristics compared to shorter wavelengths. To determine the stable wavelength range during gliding, the influence of wavelength variation on hydrodynamic forces was investigated. Simulations were conducted under the following conditions: flow

velocity of 10 m·s^{-1}, wave height of 0.5 m, glide attitude angle of 6°, and float immersion depth of 0.75 *h*. The wavelength was varied from 1 m to 15 m in increments of 2 m. The resulting transient hydrodynamic forces are presented in Fig. 16.

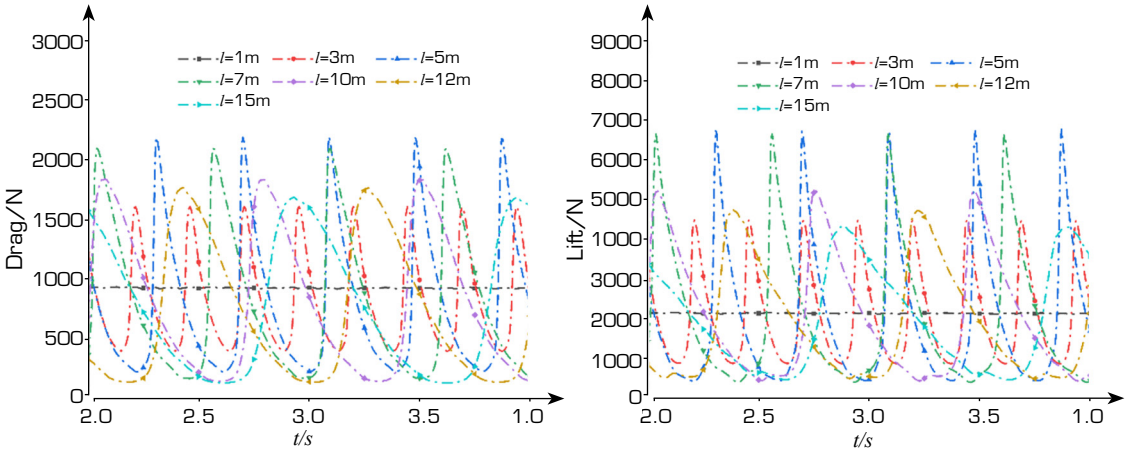

Source: Elaborated by the authors.

Figure 16. Comparative analysis of transient drag and lift forces under different wavelength conditions (wave height: 0.5 m, velocity: 10 m·s^{-1}).

Figure 16 demonstrates the variation in drag and lift acting on the float under different wavelengths. Shorter wavelengths correspond to higher wave speeds, whereas longer wavelengths are associated with lower wave speeds and extended wave periods. Similar to the effect of wave height, the impact of a wave crest on the float causes a sharp increase in both lift and drag. Notably, the lift increases more rapidly than the drag under such conditions.

Figure 17 shows that the pressure is elevated near the center of gravity of the float at a wavelength of 5 m. In contrast, at a longer wavelength (l = 10 m), the pressure is concentrated toward the front of the float. This observation is corroborated by the two-phase contours in Fig. 18. These results demonstrate that when wave crests impact the float near its center of gravity, both the drag and lift are significantly amplified.

Figure 19 shows that the clockwise vortex at the front of the float is more pronounced at a wavelength of l = 5 m, generating an upward surge flow. This enhances both the drag and lift during gliding, thereby contributing to instability. Conversely, at a wavelength of l = 10 m, the leading-edge vortex weakens significantly, resulting in considerably lower drag and lift.

When the wavelength ranges from 5 m to 7 m, the wave crest strikes the float near its center of gravity, resulting in augmented lift and drag. With increasing wavelength, the wave propagation velocity decreases. Under these conditions, the wave crest contacts the float at a more forward position, causing the clockwise vortex at the leading edge to weaken and consequently reducing both hydrodynamic forces.

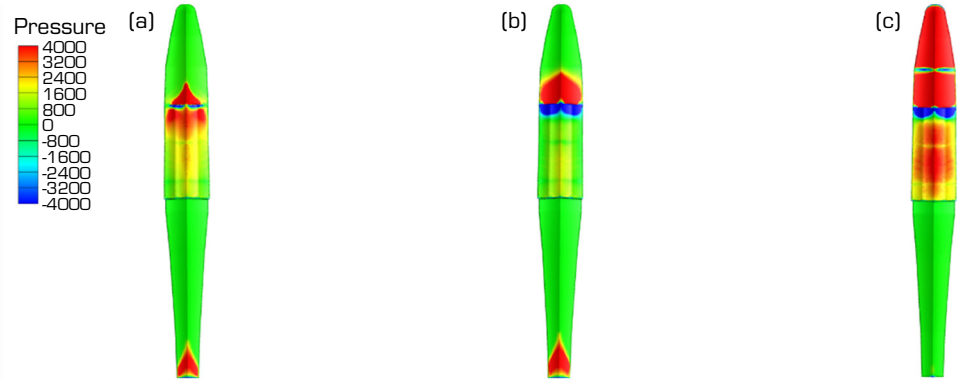

Source: Elaborated by the authors.

Figure 17. Hydrodynamic pressure patterns at float bottom for different wavelengths. (a) l = 5 m; (b) l = 7 m; (c) l = 10 m.

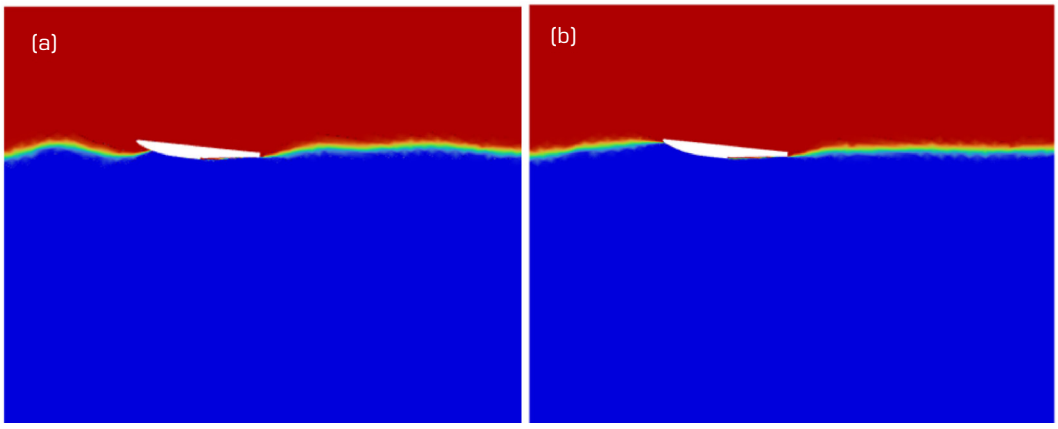

Source: Elaborated by the authors.

Figure 18. Instantaneous two-phase contours during wave-gliding (α = 0.5 m). (a) l = 5 m; (b) l = 10 m.

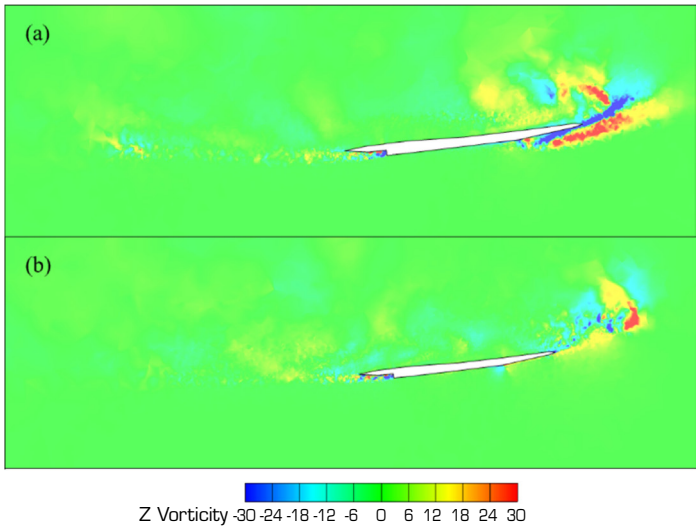

Source: Elaborated by the authors.

Figure 19. Comparison of vorticity distributions under different wavelengths at t = 5 s. (a) l = 5 m; (b) l = 10 m.

Influence of variable speed on the stability

The glide stability of amphibious aircraft on wavy water surfaces is critically influenced by speed variations during accelerated take-off and decelerated stopping. In this study, variable-speed conditions are implemented via UDF. As summarized in Table 8, five acceleration cases (from 5 m·s^{-1} to 15 m·s^{-1}) and five deceleration cases (from 15 m·s^{-1} to 5 m·s^{-1}) are defined, with the corresponding acceleration functions provided.

Theoretical analysis confirms that the variable-speed motion of the amphibious aircraft follows a trigonometric profile. Accordingly, the UDF functions listed in Table 8 are formulated to reflect this physical behavior. Under the reference conditions – a current velocity of 10 m·s^{-1}, wave height of 0.5 m, wavelength of 5 m, glide attitude of 6°, and a submersion depth of 0.75 h – the UDF-driven simulations produce the lift and drag curves during speed transitions, as shown in Figs. 20 and 21.

Figures 20 and 21 show that drag and lift increase with acceleration during wave gliding. During deceleration – modeled as a transition to 5 m·s^{-1}over a 5-second interval – both forces peak upon initial wave contact, with higher initial speeds producing more pronounced wave crest interactions. Under strong deceleration from high speed, the float may partially emerge from the water within 1-2 s, leading to a sharp reduction in hydrodynamic forces.

Table 8. Glide acceleration (V) and deceleration (P) trigonometric profiles.

Velocity change in 5 s	Acceleration function	Deceleration function
V1 (5 m·s^{-1}-6 m·s^{-1}) P1 (6 m·s^{-1}-5 m·s^{-1})	$5.5+0.5\times\sin(\frac{\pi}{5}\times time-\frac{\pi}{2})$	$5.5+0.5\times\cos(\frac{\pi}{5}\times time)$
V2 (5 m·s^{-1}-8 m·s^{-1}) P2 (8 m·s^{-1}-5 m·s^{-1})	$6.5+1.5\times\sin(\frac{\pi}{5}\times time-\frac{\pi}{2})$	$6.5+1.5\times\cos(\frac{\pi}{5}\times time)$
V3 (5 m·s^{-1}-10 m·s^{-1}) P3 (10 m·s^{-1} 5 m·s^{-1})	$7.5+2.5\times\sin(\frac{\pi}{5}\times time-\frac{\pi}{2})$	$7.5+2.5\times\cos(\frac{\pi}{5}\times time)$
V4 (5 m·s^{-1}-12 m·s^{-1}) P4 (12 m·s^{-1}-5 m·s^{-1})	$8.5+3.5\times\sin(\frac{\pi}{5}\times time-\frac{\pi}{2})$	$8.5+3.5\times\cos(\frac{\pi}{5}\times time)$
V5 (5 m·s^{-1}-15 m·s^{-1}) P5 (15 m·s^{-1}-5 m·s^{-1})	$10+5\times\sin(\frac{\pi}{5}\times time-\frac{\pi}{2})$	$10+5\times\cos(\frac{\pi}{5}\times time)$

Source: Elaborated by the authors.

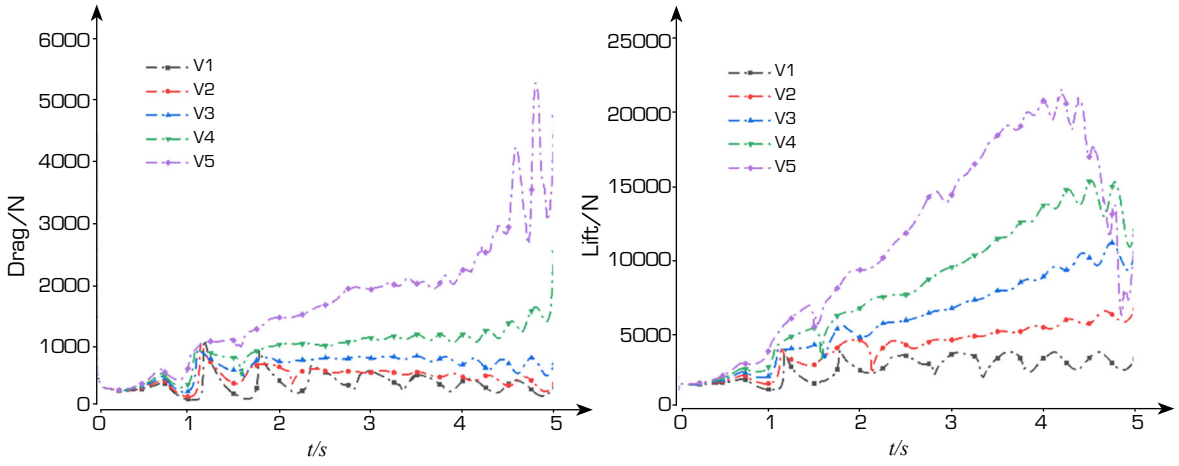

Source: Elaborated by the authors.

Figure 20. Evolution of transient forces during acceleration gliding under l = 0.5 m and h = 0.5 m.

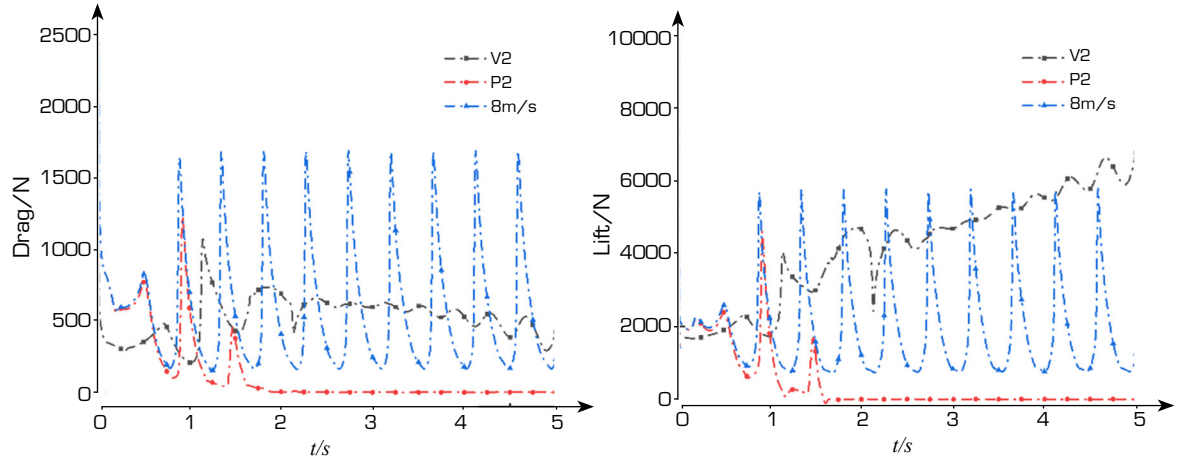

Source: Elaborated by the authors.

Figure 21. Time history of lifts and drags under different gliding modes: variable-speed conditions and steady 8 m·s^{-1}gliding.

Figure 22 compares the lift and drag forces during steady gliding at 8 m·s^{-1} with those under accelerated (V2) and decelerated (P2) conditions. The results show that both forces vary periodically and consistently during steady gliding, whereas transient fluctuations occur during acceleration and deceleration. Analysis of the acceleration phase reveals distinct changes in the lift and drag curves at approximately t = 2 s and 2.5 s. The corresponding two-phase flow structures and vortex patterns at these instants are presented in Figs. 23 and 24.

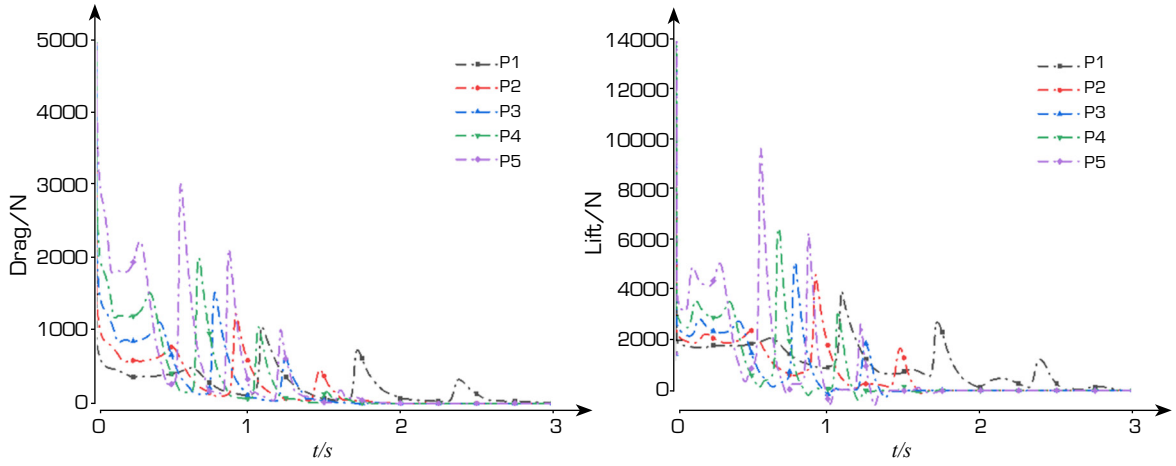

Source: Elaborated by the authors.

Figure 22. Hydrodynamic forces during deceleration phases (velocity: 15-5 m·s^{-1}; wave parameters: α = 0.5 m, λ = 5 m).

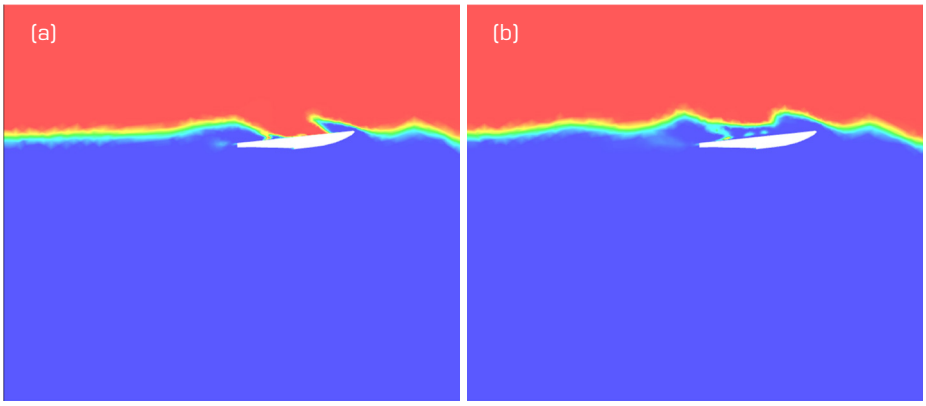

Source: Elaborated by the authors.

Figure 23. Evolution of the air-water interface during acceleration phase (V2). (a) t = 2 s; (b) t = 2.5 s.

Figure 24 illustrates that during rapid gliding, the negative vortex at the float's head is larger than the positive vortex, resulting in comparatively lower resistance throughout the operation than in uniform gliding. At t = 2 s, the float's bow generates numerous negative vortices, leading to the separation of water flow at the vessel's fore, as illustrated by the phenomenon at t = 2 s in Fig. 23. This separation complicates the frictional resistance during the float's gliding process. The alteration in the water's velocity gradient influences the magnitude of the frictional resistance, resulting in a temporary reduction. However, following the separation, a low-pressure zone forms behind the float's head. Following separation, a low-pressure zone will develop behind the float's head, while the head remains a high-pressure zone. According to Bernoulli's principle, this phenomenon increases shape resistance. Concurrently, the negative vortex at the float's front redistributes the water flow distribution, thereby increasing both frictional and wave resistance, culminating in an overall rise in resistance at the float's moment of 2 s -2.5 s.

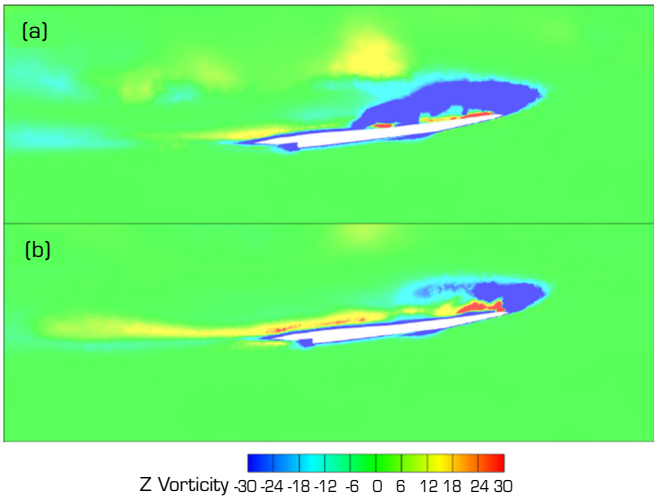

Source: Elaborated by the authors.

Figure 24. Transient evolution of vortex patterns during V2 accelerated gliding (α = 0.5 m, λ = 5 m). (a) t = 2 s; (b) t = 2.5 s.

The location and strength of the front negative vortex vary with the gliding state, modifying flow pressure and velocity. This reduces effective lift and causes instability, explaining the sharp drop in lift at t = 2 s. By t = 2.5 s, the negative vortex weakens while the tail positive vortex intensifies. The float rises above the water, and the trailing vortex produces thrust that accelerates flow at the stern. The consequent pressure drop (Bernoulli's principle), together with higher pressure on the upper surface, enhances lift. Meanwhile, forward acceleration induces a positive vortex that pushes against the water; the reaction force (Newton's third law) further modifies the flow and causes water accumulation ahead of the float.

When the accelerating float interacts with waves, its motion amplifies wave deformation. During a wave trough, forward thrust combines with upward wave motion, increasing surface convexity. During a wave peak, acceleration disturbs wave propagation, sharpening the crest and enhancing water pooling. These interactions collectively raise the local water surface during gliding and disrupt periodic force variations.

During the deceleration phase, both drag and lift decrease over time, as shown in Fig. 22. In cases of more pronounced deceleration, these forces drop to near-zero levels within 1-2 seconds. This behavior is further illustrated in the two-phase and vorticity contours in Figs. 25 and 26. The figures confirm that as the float decelerates on the wavy surface, the positive and negative vortices at its front end dissipate following wave crest impact at t = 1 s. This vortex breakdown leads to a simultaneous

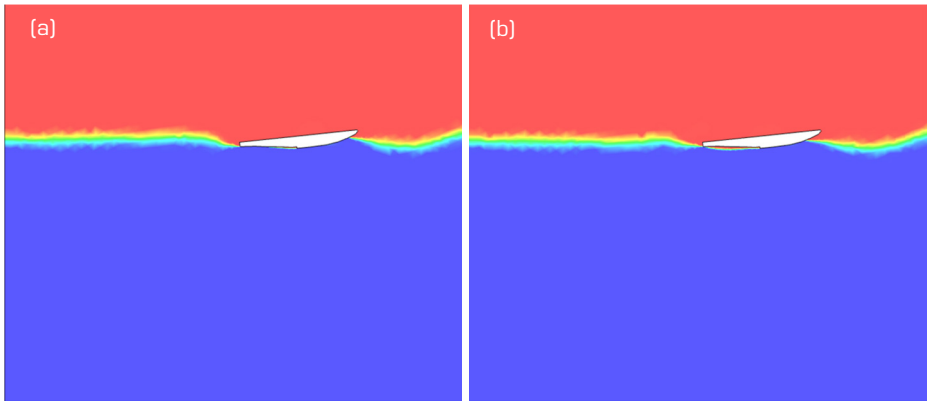

Source: Elaborated by the authors.

Figure 25. Transient two-phase flow patterns during P2 deceleration gliding (wave parameters: α = 0.5 m, λ = 5 m). (a) t = 1 s; (b) t = 1.5 s.

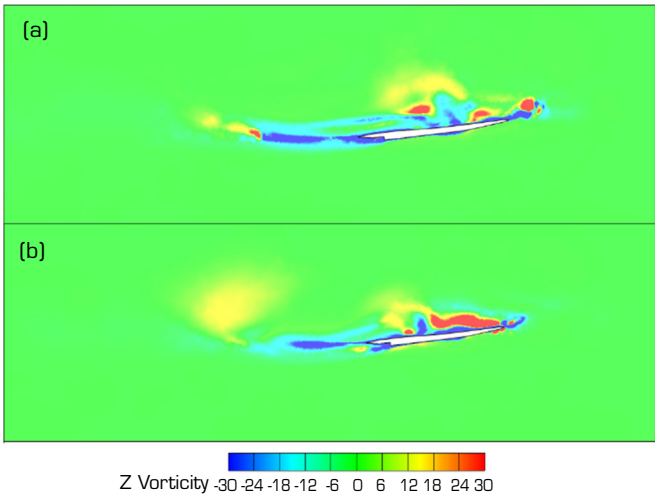

Source: Elaborated by the authors.

Figure 26. Vortex structure development during P2 deceleration phase (velocity: 15-1 m·s^{-1}). (a) t = 1 s; (b) t = 1.5 s.

decrease in both hydrodynamic forces. After t = 1.5 s, the water surface falls away from the float, resulting in further separation and near-elimination of drag and lift. Any residual oscillation of the force curves around zero is attributed to aerodynamic effects acting on the exposed float.

As shown in Fig. 26, the observed water surface depression primarily results from vortex-induced flow separation. Vortex shedding drives fluid radially outward, and according to mass conservation in incompressible flow, the horizontally displaced water is compensated by a vertical downward flow into the vortex core, leading to localized surface lowering. Bernoulli's principle further explains that the increased velocity and corresponding pressure reduction at the vortex center promote inward flow from surrounding higher-pressure regions, which also contributes to surface depression. In a wavy environment, this vortex-induced pressure field interacts with wave motion. Although vortex rotation in the simulation has limited spatial influence, it can still cause a significant local surface drop. Meanwhile, wave undulations modulate the effect: at wave crests (e.g., t = 1.5 s in Fig. 25), upward wave motion can partially offset the vortex-induced sinking, whereas at troughs, the descending effect may be amplified. Factors such as float acceleration, submersion depth, glide attitude, and wave parameters also affect surface elevation, though these are not analyzed in detail here.

Vortex shedding generates transverse asymmetric loads, causing roll motions and local upward/downward forces on opposite sides of the float. Concurrently, rapid deceleration alters the bow flow distribution, leading to trim changes, such as bow up or bow down pitching, which significantly affect longitudinal stability.

During accelerated or decelerated taxiing, the light electric amphibious aircraft is subject to yawing moments, roll motions, and pitch variations induced by changes in hydrodynamic forces and vortex patterns, which significantly disturb the surrounding flow field.

CONCLUSION

This study investigates the gliding stability of a light amphibious aircraft during taxiing on wavy water, focusing on the effects of wave height, wavelength, and variable-speed conditions. A comparative analysis was conducted to evaluate aircraft response under various operational scenarios.

The results indicate that at a wave height of 0.5 m, wave pressure concentrates near the float's center of gravity, causing a sharp increase in transient lift and drag. When the wave height exceeds 1 m but remains below 1.5 m, wave forces act predominantly on the midsection of the float, leading to a reduction in both lift and drag. A further increase in wave height allows the wave trough to impact the float, resulting in renewed growth in hydrodynamic forces. At a wavelength of 5 m, wave impact occurs near the center of gravity, simultaneously elevating lift and drag. With increasing wavelength, the wave period elongates, reducing the

frequency of wave–float interactions. Concurrently, lower wave velocities lead to more gradual variations in lift and drag. Both a wave height of 0.5 m and a wavelength of 5 m represent critical conditions that can induce longitudinal oscillations during taxiing. In addition, speed variation is shown to significantly influence aircraft hydrodynamic behavior and stability. The UDF-controlled acceleration scheme provides a precise method to actively perturb the flow field. This controlled intervention directly modulates hydrodynamic loads (lift and resistance) and induces yawing moments, thereby enabling a systematic investigation of its effects on both lateral and longitudinal stability during float glide. This study offers a research concept for examining the stability of light amphibious aircraft floats navigating over waves.

CONFLICTS OF INTEREST

Nothing to declare.

AUTHOR CONTRIBUTIONS

Conceptualization: Zhandong L; **Methodology:** Zhandong L and Feifan Z; **Software:** Feifan Z; **Validation:** Feifan Z; **Formal analysis:** Zhandong L and Feifan Z; **Investigation:** Zhandong L and Feifan Z; **Resources:** Zhandong L and Feifan Z; **Data Curation:** Zhandong L and Feifan Z; **Writing – Original Draft:** Feifan Z; **Writing – Review & Editing:** Zhandong L and Feifan Z; **Visualization:** Feifan Z; **Supervision:** Zhandong L, Fanwei K, Ligang Q, and Jinfang Z; **Project Administration:** Zhandong L, Fanwei K, Ligang Q, and Jinfang Z; **Final approval:** Zhandong L.

DATA AVAILABILITY STATEMENT

All data sets were generated or analyzed in the current study.

FUNDING

Joint Program Project of Natural Science Foundation of Liaoning Province
Grant No: 2025-MSLH-560

Liaoning Provincial Department of Education Fund Project
Grant No: JYTMS20230282

The Fundamental Research Funds for the Universities of Liaoning Province
Grant No: LJ212410143100

DECLARATION OF USE OF ARTIFICIAL INTELLIGENCE TOOLS

In writing this paper, the author used artificial intelligence tools for translation between Chinese and English and for checking grammar. The author assumes full responsibility for the use of these tools and bears full responsibility for the content of the paper.

ACKNOWLEDGMENTS

Not applicable.

REFERENCES

Che X (2022) Research on modeling design of lightweight electric amphibious aircraft (undergraduate thesis). Shenyang: Shenyang Aerospace University.

Chen J, Xiao T, Wang M, Tong M (2022) Numerical study of wave effect on aircraft water-landing performance. Applied Sciences 12(5):2561.https://doi.org/10.3390/app12052561

Duan XP, Sun WP, Wei M (2019) Numerical simulation of amphibious aircraft taxiing at high speed on water using OpenFOAM. Acta Aeronaut Astronaut Sin 40:522330. https://doi.org/10.7527/S1000-6893.2018.22330

Hu KY, Nan C, Shi LF, Hu S (2020) Numerical simulation study of gliding motion in regular waves of amphibious aircraft. China Shipbuilding 61(S2):254-261. https://doi.org/10.3969/j.issn.1000-4882.2020.z2.028

Huang HM (2018) Research on the current status and development of amphibious light sport aircraft technology. Value Engineering 37(21):124-125. https://doi.org/10.14018/j.cnki.cn13-1085/n.2018.21.053

Huang M, Chu L, Li C, Jiang R, Tang B, Wu B (2019) Seakeeping performance research of large amphibious aircraft. Acta Aeronaut Astronaut Sin 40:522–535. https://doi.org/10.7527/S1000-6893.2018.22335

Huang M, Lian Z, Zuo Z, Wang G (2016) Study of scaled model tank tests in waves of an amphibian. Aeronaut Sci Technol 27:74–78. https://doi.org/10.3969/j.issn.1007-5453.2016.01.015

Huang M, Wu B, Jiang R, Jiao J (2015) Experimental study on motion response of a seaplane on waves. J Exp Fluid Mech 29:41-46. https://doi.org/10.11729/syltlx20140104

Ju AR, Sun WP, Sun HW, Qin JC, Yang G (2020) Hydrodynamic characterization of amphibious aircraft taxiing on wavy water. Marine Engineering 42(10):47-55. https://doi.org/10.13788/j.cnki.cbgc.2020.10.09

Kajitani H, Miyata H, Ikehata M (1983). The summary of the cooperative experiment on Wigley parabolic model in Japan. Tokyo: University of Tokyo.

Li W, Gao XJ, Huang M, Zang Y (2023) Numerical simulation of wave loads on amphibious aircraft. Ship Science and Technology 45(8):31-34. https://doi.org/10.3404/j.issn.1672-7649.2023.08.007

Li XY, Cai K, Wang LL (2019) Numerical calculation and experimental analysis of high-speed water surface planning performance of amphibious aircraft. Phys Gases 4:56–62. https://doi.org/10.19527/j.cnki.2096-1642.0781

Li XY, Wang MZ, Tang BB (2020a) Numerical calculation and water tank testing of high-performance composite hull wave resistance for amphibious aircraft. Sci Technol Eng 20:2099–2104.

Li XY, Wu B, Jiang R (2020b) Numerical simulation of wave resistance for single-hull amphibious aircraft based on sliding mesh method. Ship Ocean Eng 49:14–18. https://doi.org/10.3963/j.issn.1671-7953.2020.03.004

Lin YP (2010). China steps up development of amphibious aircraft. Traffic and Transportation 26(1):31-33.

Lv J, Yang SF, Yang R, Zang Y (2023) Current status and development of hydrodynamic strength technology for amphibious aircraft. Aviation Manufacturing Technology 66(6):74-84. https://doi.org/10.16080/j.issn1671-833x.2023.06.074

Ma ZH, Liu LS, Zhu GF, Wang X (2018) Research on the dynamic characteristics of amphibious aircraft landing on wavy water surface. Computer Simulation 35(7):41-45.

Shi LF (2024) Research on gliding motion and landing and takeoff characteristics of amphibious aircraft in waves (undergraduate thesis). Harbin: Harbin Engineering University. https://doi.org/10.27060/d.cnki.ghbcu.2022.000680

Sun H, Ju A, Chang W, Liu J, Liu J, Sun H (2024) Research on wave-added resistance and longitudinal stability characteristics of amphibious aircraft in rule wave. J Mar Sci Eng 12(4):585. https://doi.org/10.3390/jmse12040585

Zeng Y, Yang SF, Luo LY (2015) Research on wave landing response of amphibious aircraft. Mech Des 32(9):96-100. https://doi.org/10.13841/j.cnki.jxsj.2015.09.019

Zhang L, Cheng YS, Wang FX (2018) Performance analysis of water-air coupling during hydrostatic takeoff of seaplane. Science Technology and Engineering 18(11):190-195.

Zhao LJ, Tian MW, Li K., Wang MY, Liu D (2021). Float design and takeoff taxiing of a waterborne electric airplane. Acta Aeronaut Astronaut Sin 42(3):41-52. https://doi.org/10.7527/S1000-6893.2020.24590

Zhou H, Hu K, Mao L, Cao J (2023). Research on planning motion and stability of amphibious aircraft in waves based on Cartesian grid finite difference method. Ocean Engineering 272:113848. https://doi.org/10.1016/j.oceaneng.2023.113848